PHYSICAL REVIEW RESEARCH **5**, 033184 (2023)

Simulating one-dimensional quantum chromodynamics on a quantum computer: Real-time evolutions of tetra- and pentaquarks

Yasar Y. Atas,[1,2,*,†] Jan F. Haase,[1,2,3,*,‡] Jinglei Zhang,[1,2,§] Victor Wei,[1,4] Sieglinde M.-L. Pfaendler,[5]
Randy Lewis,[6] and Christine A. Muschik[1,2,7]
[1]*Institute for Quantum Computing, University of Waterloo, Waterloo, Ontario, Canada N2L 3G1*
[2]*Department of Physics & Astronomy, University of Waterloo, Waterloo, Ontario, Canada N2L 3G1*
[3]*Institut für Theoretische Physik und IQST, Universität Ulm, Albert-Einstein-Allee 11, D-89069 Ulm, Germany*
[4]*Department of Physics, McGill University, Montreal, Quebec, Canada H3A 2T8*
[5]*IBM Deutschland Research & Development GmbH, Schönaicher Straße 220, D-71032 Böblingen, Germany*
[6]*Department of Physics and Astronomy, York University, Toronto, Ontario, Canada M3J 1P3*
[7]*Perimeter Institute for Theoretical Physics, Waterloo, Ontario, Canada N2L 2Y5*

(Received 30 December 2022; accepted 20 June 2023; published 13 September 2023)

Quantum chromodynamics (QCD)—the theory of quarks and gluons—has been studied for decades, but it is yet to be fully understood. A recent example is the prediction and experimental discovery of tetraquarks, which opened a new research field. Crucially, numerous unsolved questions regarding the standard model can exclusively be addressed by nonperturbative calculations. Quantum computers can solve problems for which well-established QCD methods are inapplicable, such as real-time evolution. We take a key step in exploring this possibility by designing a real-time evolution of tetraquark and pentaquark physics in one-dimensional SU(3) gauge theory. We also perform an experiment on a superconducting quantum computer demonstrating an elementary cell consisting of two staggered sites containing quarks and antiquarks with all three colors. This experiment represents an exciting step in quantum computation involving quarks with the gauge group of QCD.

DOI: 10.1103/PhysRevResearch.5.033184

I. INTRODUCTION

Quantum chromodynamics (QCD) provides the fundamental understanding of the strong nuclear force. It describes a vast range of hadrons and their properties in terms of just the quark masses and a gauge coupling. The recent discoveries [1] of several tetraquark candidates are reminders of the richness still remaining to be understood within QCD.

Lattice gauge theory is the first-principles nonperturbative theoretical tool for studying QCD. Emerging quantum computers will allow lattice studies to access new topics within QCD, such as real-time evolution [2–4]. In this paper, we use real-time evolution to present a study of tetraquarks and pentaquarks on a quantum computer. Our calculations use SU(3) gauge theory in one spatial dimension [5], and the number of qubits (entangling gates) required scales only linearly (quadratically) in the number of lattice sites N. To match the available quantum hardware, our experimental demonstrations focus on a lattice of minimal length, i.e., the basic building block.

Previous quantum computations within U(1) gauge theory [6–14] showed electron-positron pair production. Moving from this simple Abelian case to a more complex non-Abelian theory reveals qualitatively new phenomena. For example, in addition to quark-antiquark pair production (and the existence of a meson), there is also a gauge-singlet particle having valence quarks without valence antiquarks (i.e., the baryon). A recent paper [15] presented the quantum computation of a baryon mass in a SU(2) gauge theory.

In this paper we consider SU(3), which is the gauge group of QCD, and demonstrate color-neutral objects (also called gauge singlets). Color-neutral states of SU(3) are invariant under arbitrary rotations in color space and thus involve all the color components (charges) available in the theory, i.e., red, green, and blue (and their anticolor counterparts). This is in contrast to Abelian quantum electrodynamics (QED), where a singlet state involves electron-positron pairs only. Since the color singlet states are the relevant physical states, their study and simulation constitute an important step towards the understanding, description, and prediction of more complex and realistic experiments.

In order to study the properties and interactions of the gauge singlets, we perform two experiments. First, we perform a quantum simulation of the tetraquark. Specifically, we identify the state possessing two quarks in a color antitriplet plus two antiquarks in a color triplet. The mixing of this state with a baryon-antibaryon pair and with other quantum states

---

[*] These authors contributed equally to this work.
[†] yasar.yilmaz.atas@gmail.com
[‡] jan.frhaase@gmail.com
[§] jingleizl@gmail.com

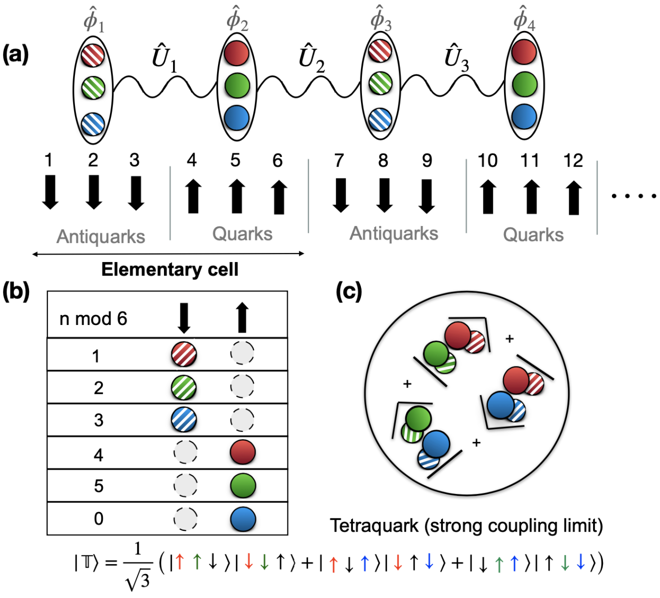

$$|\mathbb{T}\rangle = \frac{1}{\sqrt{3}}\left(|\uparrow\uparrow\downarrow\rangle|\downarrow\downarrow\uparrow\rangle + |\uparrow\downarrow\uparrow\rangle|\downarrow\uparrow\downarrow\rangle + |\downarrow\uparrow\uparrow\rangle|\uparrow\downarrow\downarrow\rangle\right)$$

FIG. 1. Gauge theory on the lattice. In order to study the SU(3) gauge theory in one dimension, we use the lattice shown in (a), where space is discretized into unit cells that each hold up to three quarks (red, green, blue) represented by filled circles and up to three antiquarks (antired, antigreen, antiblue) represented by striped circles. Each unit cell is connected to the neighboring one with a gauge link $\hat{U}_i$. Each particle represented by the fermionic field $\hat{\phi}_n^i$ ($i = 1, 2, 3$) is mapped to a qubit according to the staggerization table in (b), where n is the index of the qubit. As an example, (c) shows a pictorial representation of the tetraquark state for an elementary cell in the strong coupling limit (consisting of a quantum superposition of orthogonal basis states), along with its spin representation (see text for details).

is extracted from the quantum computation of time evolution. Second, we study a pentaquark by considering two quark flavors of different masses. Taking the infinite-mass limit for the second flavor allows us to perform an experiment showing oscillations between a pentaquark and a baryon.

Very recent quantum simulations of SU(2) and SU(3) gauge theories for particle physics [15–23] have succeeded in accessing increasingly complex model systems on the route towards QCD. Our experiment takes this quest a crucial step forward by arriving at the simulation of physical states of SU(3) relevant for hadron physics experiments.

II. THEORY

A. SU(3) gauge theory

Our calculations use the Hamiltonian approach where time is not discretized, and the lattice is purely spatial. We consider a one-dimensional (1D) lattice with open boundary conditions, where each site n hosts a fermionic field with three color components, $\hat{\boldsymbol{\phi}}_n = (\hat{\phi}_n^1, \hat{\phi}_n^2, \hat{\phi}_n^3)^{\mathrm{T}}$. We choose to work with staggered fermions [24] with the convention that odd sites host antimatter, while even sites host matter, as shown in Fig. 1(a). The gauge fields are defined on the link between sites n and $n+1$ and mediate the interaction between color degrees of freedom. The gauge-invariant lattice Hamiltonian in natural units ($\hbar = c = 1$) reads

$$\hat{H}_l = \frac{1}{2a}\sum_{n=1}^{N-1}(\hat{\phi}_n^{\dagger}\hat{U}_n\hat{\phi}_{n+1} + \mathrm{H.c.}) + m\sum_{n=1}^{N}(-1)^n\hat{\phi}_n^{\dagger}\hat{\phi}_n + \frac{ag^2}{2}\sum_{n=1}^{N-1}\hat{\mathbf{L}}_n^2, \tag{1}$$

where "H.c." denotes the Hermitian conjugate, N is the number of lattice sites with spacing a, m is the quark bare mass, and g is the bare coupling. The first term in the Hamiltonian describes the creation of particle-antiparticle pairs with $\hat{U}_n$ being the corresponding gauge operator adapting the gauge field during pair creation. The second term is the mass term (the alternating sign appearing here is the signature of the staggered formulation). The last term encodes the color electric energy of the system and is expressed in terms of the left color electric field $\hat{\mathbf{L}}_n$ on the link n. Furthermore, it is convenient to introduce the non-Abelian charges at site n, $\hat{Q}_n^a = \sum_{i,j=1}^{3}\hat{\phi}_n^{i\dagger}(T^a)_{ij}\hat{\phi}_n^j$, where $T^a = \lambda^a/2$ and λ^a ($a = 1, \ldots, 8$) are the Gell-Mann matrices [25]. These charges appear in the non-Abelian version of the Gauss law that physical states must satisfy [26]. We work in the sector with zero external charges and zero total non-Abelian charge, i.e., a color singlet state must satisfy $\hat{Q}_{\mathrm{tot}}^a|\Psi\rangle \equiv \sum_n \hat{Q}_n^a|\Psi\rangle = 0$. Besides the eight non-Abelian charges, the Hamiltonian also conserves the baryon number B, which measures the matter-antimatter imbalance (see Appendix A 1). In our first study, we target tetraquark physics and are therefore interested in the $B = 0$ subsector where all states contain an equal number of quarks and antiquarks. In our second study we target pentaquark physics and consider therefore the sector with $B = 1$.

B. Effective qubit formulation

To simulate and study the rich physics of the SU(3) theory, we encode Eq. (1) in a Hamiltonian suitable for quantum simulations. In a first step, a gauge transformation is applied to eliminate the gauge degrees of freedom from the Hamiltonian, allowing us to express the Hamiltonian in terms of fermions only [27]. This first step is applied to save resources (as gauge fields are not stored explicitly in the qubit register) at the expense of introducing long-range interactions. In a second step, a Jordan-Wigner transformation [28] translates fermionic matter degrees of freedom into spin $\frac{1}{2}$, i.e., qubit degrees of freedom (see Fig. 1). It is convenient to rescale the Hamiltonian with the lattice spacing a, resulting in

$$\hat{H} = \hat{H}_{\mathrm{kin}} + \tilde{m}\hat{H}_m + \frac{1}{2x}\hat{H}_e, \tag{2}$$

where $\tilde{m} = am$ and $x = 1/(ga)^2$ are the dimensionless mass and coupling constant, respectively. In the spin formulation, the kinetic term is given by

$$\hat{H}_{\mathrm{kin}} = \frac{1}{2}\sum_{n=1}^{N-1}(-1)^n\big(\hat{\sigma}_{3n-2}^{+}\hat{\sigma}_{3n-1}^{z}\hat{\sigma}_{3n}^{z}\hat{\sigma}_{3n+1}^{-} - \hat{\sigma}_{3n-1}^{+}\hat{\sigma}_{3n}^{z}\hat{\sigma}_{3n+1}^{z}\hat{\sigma}_{3n+2}^{-} + \hat{\sigma}_{3n}^{+}\hat{\sigma}_{3n+1}^{z}\hat{\sigma}_{3n+2}^{z}\hat{\sigma}_{3n+3}^{-} + \mathrm{H.c.}\big), \tag{3}$$

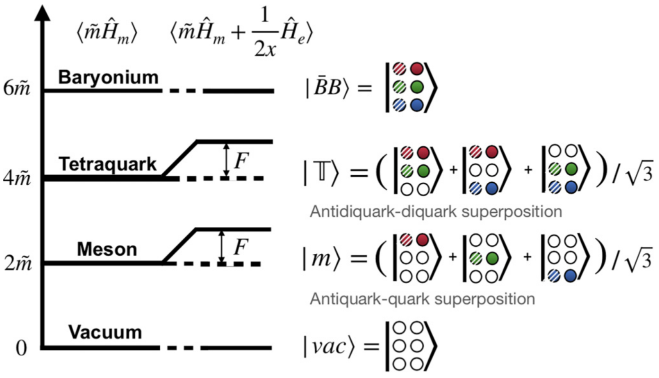

FIG. 2. Strong coupling states. The energy eigenstates in the strong coupling limit form a convenient basis for $N = 2$ lattice sites (see text for more details). For the basic building block of the lattice (see Fig. 1), these are given by the bare vacuum $|\text{vac}\rangle$, meson $|m\rangle$, tetraquark $|\mathbb{T}\rangle$, and baryon-antibaryon (baryonium) $|\bar{B}B\rangle$. The meson and tetraquark both carry one unit of electric flux $F = \frac{4}{3} \times \frac{1}{2x}$ for SU(3); this is indicated by the energy splitting in presence of the electric field term $\hat{H}_e$. We resort to a two-column representation for the states in the fermion occupation number basis, where the first and second columns indicate the state of the antimatter and matter, respectively.

and the mass term reads

$$\hat{H}_m = \frac{1}{2}\sum_{n=1}^{N}\left[(-1)^n\left(\hat{\sigma}^z_{3n-2} + \hat{\sigma}^z_{3n-1} + \hat{\sigma}^z_{3n}\right) + 3\right]. \qquad (4)$$

The operators $\hat{\sigma}^x = (\hat{\sigma}^- + \hat{\sigma}^+)$, $\hat{\sigma}^y = i(\hat{\sigma}^- - \hat{\sigma}^+)$, and $\hat{\sigma}^z$ are the usual Pauli matrices. The color electric field Hamiltonian takes the form

$$\hat{H}_e = \sum_{n=1}^{N-1}\left(\sum_{m\leqslant n}\hat{\mathbf{Q}}_m\right)^2, \qquad (5)$$

where $\hat{\mathbf{Q}}_m$ is a vector with eight components given by the non-Abelian charges at site m. The expression of the non-Abelian charges in terms of qubit operators can be found in Appendix A 1. In Sec. III C we use this equation to simulate the time evolution of the electric field energy.

III. QUANTUM SIMULATION AND RESULTS

In the following, we describe our quantum simulation approach first for the tetraquark study and then for the pentaquark study. For both, we focus on the basic building block consisting of $N = 2$ lattice sites (the scaling analysis for larger lattices is given in Appendix B 2). A convenient basis is the strong coupling one given by $\tilde{m} \to \infty$ and $x \to 0$, i.e., in the limit in which $\hat{H}_m$ and $\hat{H}_e$ dominate over the kinetic term $\hat{H}_{\text{kin}}$. The gauge-invariant (color-neutral) basis states in that limit can be constructed by successively applying the kinetic term to the vacuum state. The different basis states obtained for $B = 0$ are depicted in Fig. 2 in the fermion occupation basis, where the first and second columns of the ket describe the antimatter and matter content of the state, respectively. While all of them possess the same quantum baryon number, the numbers of particle-antiparticle pairs contained in them differ. These states are all eigenstates of the mass Hamiltonian given in Eq. (4), which counts the number of particles and antiparticles in a state, with integer eigenvalues 0, 2, 4, and 6 for the vacuum, meson, tetraquark, and baryon-antibaryon states, respectively. The meson state consists of a color-singlet superposition of particle-antiparticle pairs. By contrast the tetraquark state is a color superposition of diquark-antidiquark pairs. Like a single antiquark, the diquark is a color antitriplet state.

At finite coupling x and mass $\tilde{m}$, the eigenstates of the Hamiltonian are given by a superposition of the strong coupling basis states. By studying time evolution under the Hamiltonian in Eq. (2), we can probe the transitions between the different eigenstates. In particular, by choosing the initial state as the strong coupling limit baryon-antibaryon state (containing six particles and antiparticles in total) and in the regime where $x/\tilde{m} \leqslant 1$, we can probe a single transition between the baryon-antibaryon state and the tetraquark state [see Fig. 3(a)]. When the parameters are chosen outside of this regime, more than one transition becomes involved in the time evolution, which makes the dynamics richer and more complex.

The time evolution is obtained from a Trotter decomposition [30] that we optimize for minimal gate depth [Fig. 6 in Appendix B shows the Trotter circuit for a basic building block ($N = 2$)]. While this minimal lattice is described by six spins (compare Fig. 1), we can simulate the $B = 0$ sector using only three qubits, due to the existence of a particle-antiparticle symmetry (see Appendix A 1). We are interested in tracking the particle number expectation value

$$\langle \hat{\mathcal{N}}(t)\rangle = \langle \Psi_0|\, e^{it\hat{H}^{(3)}}\hat{H}^{(3)}_m e^{-it\hat{H}^{(3)}}\,|\Psi_0\rangle\,, \qquad (6)$$

as we evolve the system in time starting from an initial state $|\Psi_0\rangle$, with $\hat{H}^{(3)}$ being the three-qubit Hamiltonian derived in Appendix A 2 and given in Eq. (A22). We focus here on $|\Psi_0\rangle = |\bar{B}B\rangle$, the baryon-antibaryon state in the strong coupling limit (see Fig. 2). In terms of spins, the strong coupling baryon-antibaryon state is given by $|\Psi_0\rangle = |\downarrow\downarrow\downarrow\rangle\,|\uparrow\uparrow\uparrow\rangle$, where the first ket refers to antiquarks and the second refers to quarks (note that only the first ket is implemented in the quantum simulation and the second is implied, as explained in Appendix A 1).

For our pentaquark study, we consider two quark flavors, with light and heavy quark masses $\tilde{m}$ and $\tilde{M}$, respectively [see Fig. 4(a)]. This scenario can be treated with full generality with quadratic scaling in the required resources. However, to allow for the observation of pentaquark physics on currently available quantum processors, we further reduce the resource requirements by introducing the following steps. We assume $\tilde{M} \gg \tilde{m}$, such that the heavy quarks can be treated in the infinite-mass limit $\tilde{M} \to \infty$. In this case, the heavy quarks in the model become stationary, i.e., their motional degrees of freedom become static. These "motionally static quarks" nevertheless contribute through their dynamic color degrees of freedom.

As a concrete example, we choose to study pentaquarks with two heavy quarks [see Fig. 4(b)]. As explained in detail in Appendix A 4, we derive a modified Hamiltonian for this specific case and devise a scheme that relegates the parts of

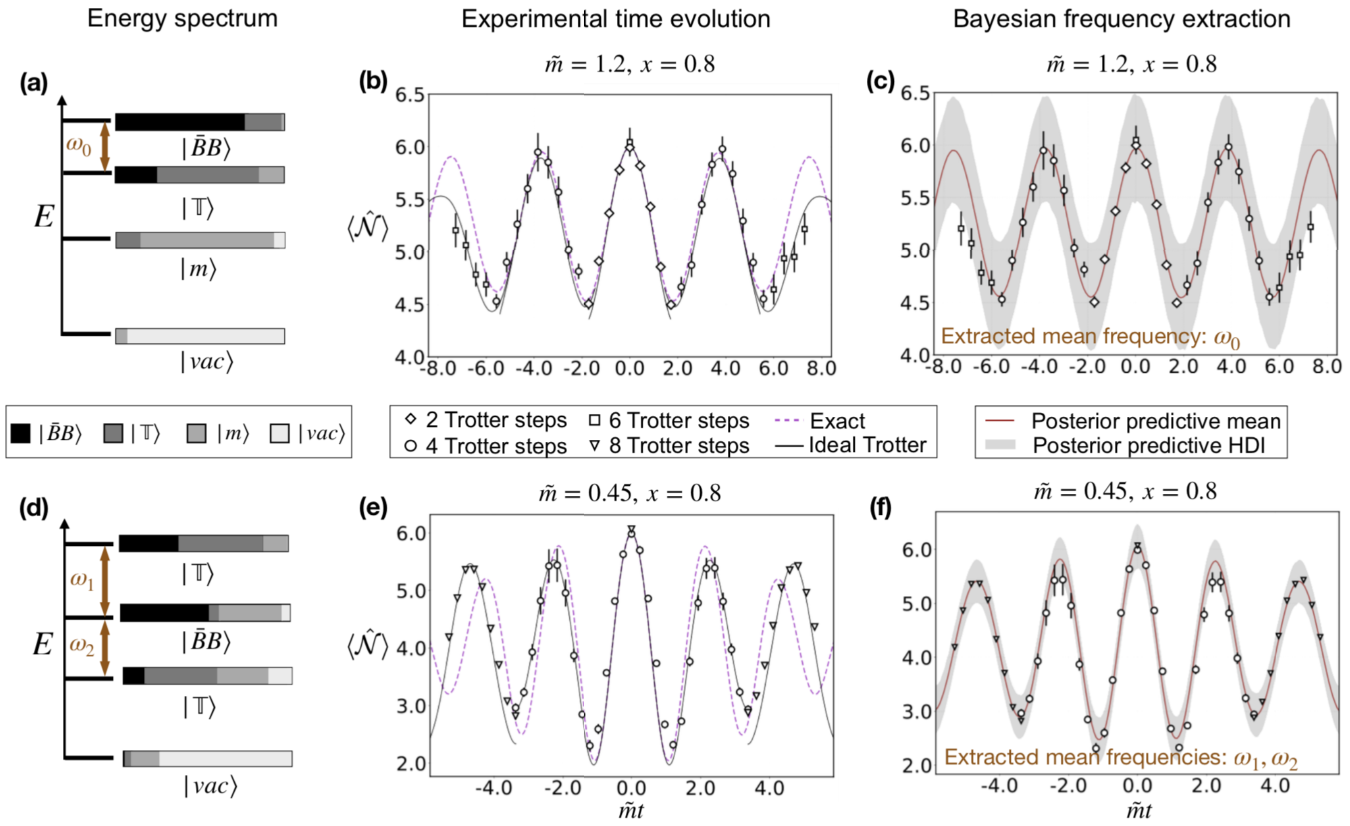

FIG. 3. Trotter time evolution with one flavor. We perform experiments for the Hamiltonian parameters $\tilde{m} = 1.2$, $x = 0.8$ [(a)–(c)] and $\tilde{m} = 0.45$, $x = 0.8$ [(d)–(f)]. The energy spectra on the left are shown to scale, and the bars reflect the proportion to which the strong coupling states in Fig. 2 contribute to the individual energy eigenstates. The data obtained on three different IBM quantum computers [ibm_peekskill (b); ibm_geneva for $N_\mathrm{T} = 4$ and ibmq_lima for $N_\mathrm{T} = 8$ (e)] are shown in the middle column, where the different symbols denote a different number of Trotter steps, and hence different circuit lengths. The circuit is heavily optimized (see Appendix B 1), contains $10N_\mathrm{T}$ CNOT gates, and has a total circuit depth of $25N_\mathrm{T} + 1$ after transpilation to the employed native gates. For the data points shown in the figure, the error mitigation has already been applied. The dashed lines mark the exact Trotter evolution obtained via a numerical exponentiation. We further composed an expected graph for the evolution obtained from the Trotter protocol, which is plotted as a solid black line. The error bars shown here originate via bootstrapping of the error mitigation method [29]. Error bars corresponding to the quantum projection noise are small due to the 2048 performed shots and would be hidden by the size of the symbols; hence they are not shown. To obtain the energy differences indicated by the arrows in the left column [(a) and (d)], we resort to Bayesian inference. The results are shown in (c) and (f), respectively, where the solid lines denote the mean of 5000 samples drawn from the posterior predictive distribution (see Appendix B 4). From these samples we also compute the highest density interval (HDI) equivalent, i.e., the gray area marks the interval between the 2.5 and 97.5 percentiles. The point estimate for the energy gap between $|\bar{B}B\rangle$ and $|\mathbb{T}\rangle$ (a) is given by $\omega_0 = (2\pi) \cdot 0.262/[\tilde{m}t]$ with an HDI of $(2\pi) \cdot [0.254,\ 0.267]/[\tilde{m}t]$. For the second case in (d), we find that $\omega_1 = (2\pi) \cdot 0.482/[\tilde{m}t]$ with HDI $= (2\pi) \cdot [0.409,\ 0.545]/[\tilde{m}t]$ and $\omega_2 = (2\pi) \cdot 0.427/[\tilde{m}t]$ where HDI $= (2\pi) \cdot [0.297,\ 0.502]/[\tilde{m}t]$. Values for other parameters in our probabilistic model can be found in Appendix B 3.

the calculation that do not have to be performed quantumly to a classical computer. We also show how to split the resulting time evolution into three separate color subsectors, which allows us to simulate the problem with only four qubits. As described in the next section, we apply this resource-efficient time evolution scheme to the baryon state as the initial state and observe oscillations between the baryon $|\mathbb{B}\rangle$ and the pentaquark $|\mathbb{P}\rangle$ [see Fig. 4(c)].

A. Error mitigation

For both studies, we use the self-mitigation method introduced in Ref. [20] (see Appendix B 3 for details). The basic idea is to use our quantum circuit in two ways. A “physics run” applies the desired number of Trotter steps, N_T, forward in time to reach the final time of interest. A “mitigation run” applies $N_\mathrm{T}/2$ steps forward in time followed by $N_\mathrm{T}/2$ steps backward in time, which results in a noisy experimental determination of the known initial state. Randomized compiling is used to surround the CNOT gates with Pauli gates that turn coherent errors into incoherent errors. We find that the minimum number of physics and mitigation runs can be as low as 40 each, and up to 560 depending on the quantum computing device chosen. Throughout this paper we always collect 2048 shots from a single circuit execution. As described in Ref. [20], the noisy observed outcomes measured during the mitigation runs provide an excellent error mitigation for the physics runs when compared with the true expected values. As in Ref. [15], each separate calculation is further accompanied by a set of 2^3 calibration circuits (2^4 for calculations involving the pentaquark) to estimate the transfer map mixing the true outcome probabilities into the observed ones. Let us

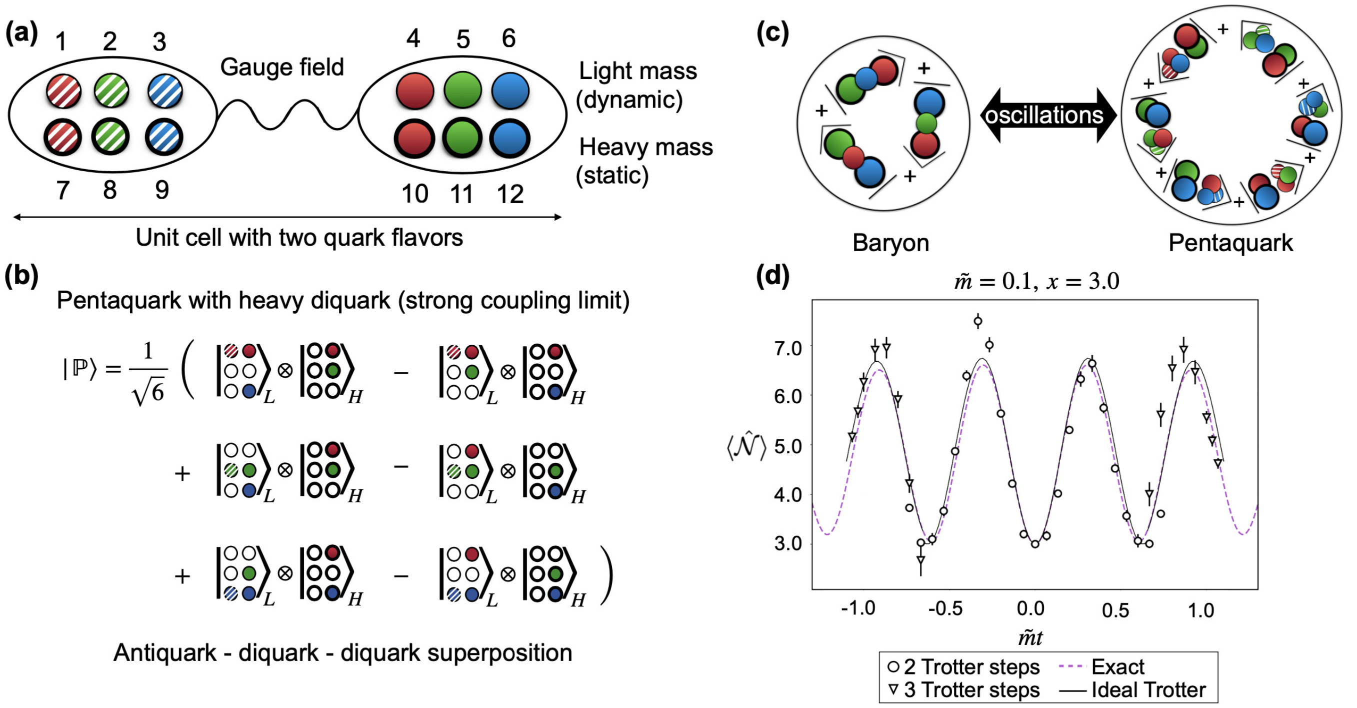

FIG. 4. Trotter time evolution with two flavors. We consider two quark flavors, with light and heavy mass, respectively. (a) The 12-qubit unit cell for this system with a gauge field connection. Circles with thick rims represent lattice sites hosting heavy quarks (lower row), which can be considered static, in contrast to the dynamic light mass quarks in the upper half of the unit cell. (b) A pentaquark state involving a heavy diquark in the strong coupling limit. (c) We simulate time evolutions that start with a baryon as the initial state and are dominated by baryon-pentaquark oscillations; the kets represent the different orthogonal basis states appearing in the quantum superposition. (d) Experimental Trotter time evolution data for $\tilde{m} = 0.1$ and $x = 3.0$. The experimental data have been obtained from ibmq_lima with two and four Trotter steps, respectively. Averaging for the error mitigation has been performed over 140 repetitions, and the results of the physical runs as well as details of the four employed qubits can be found in Appendix B 3.

remark that such a procedure is not preventing the scalability of our calculations. The increased effort using that technique is mainly influenced by the randomized compiling, which has recently been suggested to be linear in the circuit depth [31]. Furthermore, the addition of the mitigation runs increases the computational effort by a constant factor of 2, which results in an overall linear scaling of the mitigation efforts in the circuit depth.

B. Experiment

For our tetraquark study, we perform two Trotter time evolution experiments on a universal superconducting quantum computer [32] using up to eight Trotter time steps. In both experiments, the system is initialized in the strong coupling baryon-antibaryon state $|\bar{B}B\rangle$ and evolved in time under the gauge-invariant three-qubit Hamiltonian given in Appendix A 2. Since the Hamiltonian preserves the baryon number, the observed evolution remains within the $B = 0$ sector.

The first experiment is carried out for the Hamiltonian parameters $x = 0.8$ and $\tilde{m} = 1.2$ [see Eq. (2)]. This quark mass is large enough to organize the hadron spectrum in an intuitive way according to the mass: the vacuum, meson, tetraquark, and baryon-antibaryon states have energies near 0, $2\tilde{m}$, $4\tilde{m}$, and $6\tilde{m}$, respectively. For reference, Fig. 3(a) shows the spectrum and the composition of physical hadron states in terms of strong coupling states. Since we choose the strong coupling baryon-antibaryon as the initial state, quark-antiquark annihilation provides a direct connection to the tetraquark state, and indeed the collected data allow us to observe this oscillation dominating the time evolution as shown in Fig. 3(b). The experiment has been performed on the ibm_peekskill device, where for each data point we run 280 (140, 140) repetitions in the case of $N_\mathrm{T} = 4$ ($N_\mathrm{T} = 2$, $N_\mathrm{T} = 6$) for physics and mitigation runs, respectively. In Fig. 3(c) we perform a Bayesian analysis [33] to extract the frequency of the oscillation and thus calculate the mass gap between the baryon-antibaryon state and the tetraquark state (see Appendix B 4 for more details). We identify one frequency, where the point estimate is given by $\omega_0 = (2\pi) \cdot 0.262/[\tilde{m}t]$ with the highest density interval (HDI) of $(2\pi) \cdot [0.254, 0.267]/[\tilde{m}t]$, which corresponds to the energy gap between $|\bar{B}B\rangle$ and $|\mathbb{T}\rangle$. The HDI is the interval where we find 95% of the values during the sampling procedure. In Fig. 3(c) we plot 5000 samples from the posterior predictive distribution, which within the 2.5 and 97.5% quantile agrees well with the collected data.

The second experiment is carried out on ibm_geneva ($N_\mathrm{T} = 4$, 560 repetitions) and ibmq_lima ($N_\mathrm{T} = 8$, 40 repetitions), employing a smaller quark mass $\tilde{m} = 0.45$ but the same coupling constant $x = 0.8$. In this case our quantum calculation of the real-time dynamics is able to reveal two dominant energy gaps, resulting in a beat frequency which is easily visible in Fig. 3(e). Applying the same Bayesian inference techniques, we extract two frequency components $\omega_1 = (2\pi)\cdot 0.482/[\tilde{m}t]$ with HDI $= (2\pi)\cdot[0.409,\ 0.545]/[\tilde{m}t]$ and $\omega_2 = (2\pi)\cdot 0.427/[\tilde{m}t]$ where HDI $= (2\pi)\cdot[0.297,\ 0.502]/[\tilde{m}t]$, which confirms the underlying physics. In particular, the strong coupling $|\bar{B}B\rangle$ initial state is once again mixing with the strong coupling tetraquark, but this tetraquark is now a significant percentage of two physical eigenstates, as shown in Fig. 3(d).

For our pentaquark study, we turn our attention to the subsector with baryon number $B = 1$ and perform a Trotter time evolution under the four-qubit Hamiltonian $\hat{H}^{(4)}$ derived in Appendix A 4. This scenario corresponds to a situation involving two heavy quarks and up to six light quarks, as shown in Fig. 4(a). We initialize the system in the state $|\mathbb{B}\rangle$, which corresponds to a baryon consisting of two heavy quarks and one light quark [see Fig. 4(b)]. The time evolution under $\hat{H}^{(4)}$ induces pair creation processes that cause the initial state $|\mathbb{B}\rangle$ to mix with the pentaquark $|\mathbb{P}\rangle$ [see Figs. 4(b) and 4(c)] and a tetraquark-baryon pair $|\mathbb{T}b\rangle$, which consists of two heavy particles and four light particles. The latter is suppressed for our chosen parameter regime $x = 3$, $\tilde{m} = 0.1$, such that the observed dynamics is dominated by baryon-pentaquark oscillations. The corresponding experimentally calculated real-time evolution of the particle number is shown in Fig. 4(d). This computation has been performed on ibmq_lima and realizes $N_{\mathrm{T}} = 2$ and $N_{\mathrm{T}} = 4$ Trotter steps. Here, we performed around 160 repetitions to realize the full potential of the error mitigation technique.

C. Time evolution of the gauge field

Our formulation of lattice QCD involves the explicit integration of Gauss law into the Hamiltonian, which enabled us to remove the gauge degrees of freedom from the description [6,27,34,35]. However, we stress that this procedure does not restrict the access to the dynamics of the gauge field, which is now expressed in terms of the fermionic field operators. This can be deduced directly from Eq. (5), which expresses the energy of the gauge field solely via the non-Abelian charges. Note that this is indeed a direct consequence of the required gauge invariance of the system, realized by the interaction of the gauge field operators $\hat{U}_n$ and the fermionic field operators $\hat{\phi}_n$, in combination with Gauss law. The latter implies direct constraints on the quantum states of the gauge field on all links surrounding each single site and the state of matter at that site. In other words, in our case, the state of the gauge field can be deduced (up to a constant) as soon as the state of matter is known.

The form of the gauge field Hamiltonian given in Eq. (5) provides access to the gauge field on each link, when the corresponding charges $\hat{\mathbf{Q}}_n$ are measured. As an explicit example, we show the time evolution of the total gauge field Hamiltonian $\langle\hat{H}_e^{(3)}\rangle$ in Fig. 5. The dynamics shown there is complementary to the evolution of the particle number shown in Fig. 3(b), and importantly, it is deduced from the same data set. To be more precise, at time $\tilde{m}t = 0$ the system is initialized in the zero-flux baryonium state $|\bar{B}B\rangle$. The subsequent time evolution is then dominated by oscillations between the baryonium and the tetraquark states, where the latter contains one unit of electric flux, which for SU(3) is equal to 4/3. At time $\tilde{m}t \approx 2$ we observe a maximum value for the electric energy. Here, the state of the systems corresponds mostly to the tetraquark state [see Fig. 3(b)]. Note that the value of the maximum is not exactly 4/3 as mentioned above, since the time-evolved state is a superposition still containing non-negligible baryonium contributions. Equivalently, the expectation value of the electric energy does not return exactly to zero at time $\tilde{m}t \approx 4$ as the time-evolved state gets superimposed with the other contributions that are displayed in Fig. 3(a).

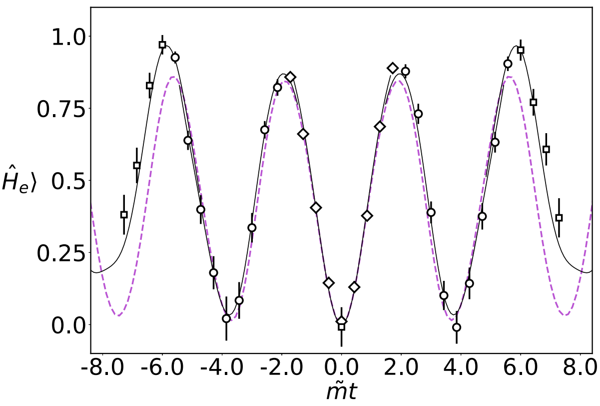

FIG. 5. Trotter evolution of the gauge fields. For the experiment shown in Fig. 3(b), where the parameters have been chosen as $\tilde{m} = 1.2, x = 0.8$, we reinterpret the measurement data and plot the energy contained in the gauge field of the time-evolved state. The system is initialized in the zero-flux baryonium state $|\bar{B}B\rangle$ and subsequently evolved in time using the three-qubit Hamiltonian derived in Appendix A. The dynamics is dominated by oscillations between the baryonium and tetraquark states containing one unit of electric flux. Full revival of the initial state is not observed due to contamination of the time-evolved state with other available basis states. Legends for the data points and the solid line are the same as in Fig. 3(b).

IV. DISCUSSION AND CONCLUSION

Recent observations of tetraquarks, pentaquarks, and other hadrons beyond the traditional mesons and baryons have sparked a great deal of theoretical activity [1], with lattice gauge theory playing a central role in the determination of static properties. To access time-dependent dynamics, we turn to the Hamiltonian approach on quantum computers.

Building on previous proposals [36–64] and demonstrations in simpler gauge theories [15–17,19–21], we have constructed a one-dimensional lattice gauge theory for QCD for two cases: one flavor of dynamical matter coupled to SU(3) gauge fields, and two flavors of matter, one of which corresponds to infinitely massive quarks. Real-time oscillations of a tetraquark and a pentaquark with other hadron states are observed by running experiments on IBM Quantum hardware [32]. Specifically, we begin from a strong coupling eigenstate at time $t = 0$ and see how the tetraquark and the pentaquark emerge. The success of these simulations required the use of recent advances in error mitigation [20].

Our approach is based on an elimination of the gauge degrees of freedom, with that physics being reexpressed as nonlocal interactions among matter fields. The general formalism developed offers a promising approach for studying larger systems, as the qubit encoding is scalable to larger lattice volumes and the CNOT count necessary to simulate the dynamics grows quadratically. Future work will extend this methodology to two (and ultimately three) spatial dimensions using the methods developed in Ref. [65]. However, such studies will require larger quantum computers with increased qubit counts and improved error mitigation techniques. This highlights the need for advancements in quantum hardware and error correction technologies for the accurate simulation of realistic QCD systems on quantum computers.

Another important route for generalizations is the extension of wider classes of simulated time evolutions to extract truly dynamical quantities. Interesting applications include time correlation functions and the ongoing quest to simulate particle collisions with quantum computers. Significant progress in quantum computer hardware and technologies is needed to tackle such problems. In particular, the development of large-scale, fault-tolerant quantum computers capable of performing complex simulations is essential. Further research and conceptual work are warranted to fully explore the potential of quantum computation in gaining new insights and addressing outstanding problems in the field of exotic hadron physics. Our simulation of SU(3) hadrons on a quantum computer accomplishes a key step on the path toward accessing increasingly relevant quantum computations for QCD.

ACKNOWLEDGMENTS

We are immensely grateful to Thomas Monz and Christian Sommer for sharing their important scientific insights and invaluable input to our project. We thank John Watrous for his support, and we are grateful for the IBM Quantum Researchers Program Access Award enabling the use of IBM Quantum services for this work. The views expressed are those of the authors and do not reflect the official policy or position of IBM or the IBM Quantum team. This research was supported by the Natural Sciences and Engineering Research Council of Canada (NSERC), the Canada First Research Excellence Fund (CFREF, Transformative Quantum Technologies), New Frontiers in Research Fund (NFRF), Ontario Early Researcher Award, and the Canadian Institute for Advanced Research (CIFAR). C.A.M. acknowledges the Alfred P. Sloan Foundation for support from a Sloan Research Fellowship. J.F.H. acknowledges the ERC Synergy Grant HyperQ (Grant No. 856432) and the BMBF Project SPINNING (FKZ:13N16215).

APPENDIX A: THEORY

1. Gauge elimination and qubit formulation

In the following, we discuss how to eliminate the gauge fields from the Hamiltonian and express it in terms of qubits only. Due to gauge invariance, the Hamiltonian in Eq. (1) commutes with the Gauss law operators (which generate the local gauge transformations) $\hat{G}_n^a \equiv \hat{L}_n^a - \hat{R}_{n-1}^a - \hat{Q}_n^a$, where $\hat{L}_n^a$ and $\hat{R}_{n-1}^a$ are the a component (with $a = 1, \dots, 8$) of the left and right color electric field defined on the link n, respectively. For a non-Abelian gauge group, the right and left color electric field are related via the adjoint representation $\hat{R}_n^a = (\hat{U}_n^{\text{adj}})_{ab}\hat{L}_n^b$, with $(\hat{U}_n^{\text{adj}})_{ab} = 2\text{Tr}[\hat{U}_n T^a \hat{U}_n^\dagger T^b]$, where $T^a = \lambda^a/2$, and λ^a $(a = 1, \dots, 8)$ are generators of the SU(3) Lie algebra and are given by the Gell-Mann matrices [25]. The Hamiltonian also commutes with the redness operator $\hat{\mathcal{R}} = \sum_{n=1}^N \hat{\phi}_n^{1\dagger}\hat{\phi}_n^1 - N/2$, the greenness operator $\hat{\mathcal{G}} = \sum_{n=1}^N \hat{\phi}_n^{2\dagger}\hat{\phi}_n^2 - N/2$, and the blueness operator $\hat{\mathcal{B}} = \sum_{n=1}^N \hat{\phi}_n^{3\dagger}\hat{\phi}_n^3 - N/2$ which measure the matter-antimatter imbalance of a specific color. It is, however, more convenient to combine these three operators into a single gauge-invariant one which measures the matter-antimatter imbalance irrespective of the color. We therefore define the baryon number operator as

$$\hat{B} = \tfrac{1}{3}(\hat{\mathcal{R}} + \hat{\mathcal{G}} + \hat{\mathcal{B}}). \tag{A1}$$

To simulate time dynamics on a quantum computer, we transform the fermionic Hamiltonian in Eq. (1) into one involving only qubit degrees of freedom. The transformation is achieved in two steps. We start by first eliminating the gauge fields following Refs. [15,27]. The resulting dimensionless Hamiltonian reads

$$\hat{H} = \frac{1}{2}\sum_{n=1}^{N-1}\sum_{i=1}^{3}(\hat{\phi}_n^{i\dagger}\hat{\phi}_{n+1}^i + \text{H.c.}) + \tilde{m}\sum_{n=1}^{N}\sum_{i=1}^{3}(-1)^n\hat{\phi}_n^{i\dagger}\hat{\phi}_n^i + \frac{1}{2x}\sum_{n=1}^{N-1}\left(\sum_{m\leqslant n}\hat{\boldsymbol{Q}}_{\boldsymbol{m}}\right)^2, \tag{A2}$$

where $\tilde{m} = am$ and $x = 1/g^2a^2$. The last term represents the color electric energy of the system and is expressed in terms of the non-Abelian charges at site n,

$$\hat{Q}_n^a = \sum_{i,j=1}^{3}\hat{\phi}_n^{i\dagger}(T^a)_{ij}\hat{\phi}_n^j. \tag{A3}$$

In a second step, we triple the size of the lattice to define $3N$ new sites and distribute the color components of the fermionic field among them by defining the single component fields $\hat{\phi}_n^i = \hat{\psi}_{3n-3+i}$ with $n = 1, 2, \dots, N$ and $i = 1, 2, 3$ [see Fig. 1(a)].

We then perform a generalized Jordan-Wigner transformation on the single component fermionic fields $\hat{\psi}_n$ [28]

$$\hat{\psi}_n = \left(\prod_{l<n} s_l\hat{\sigma}_l^z\right)\hat{\sigma}_n^-, \quad \hat{\psi}_n^\dagger = \left(\prod_{l<n} s_l\hat{\sigma}_l^z\right)\hat{\sigma}_n^+, \tag{A4}$$

where s_l are phase factors that we choose equal to $+1$ on antimatter sites and -1 on matter sites. This choice is convenient because it matches the standard color notation, such as $(\bar{r}r + \bar{g}g + \bar{b}b)/\sqrt{3}$ for a meson. After the Jordan-Wigner transformation, the kinetic Hamiltonian in terms of qubits is given by Eq. (3), while the mass Hamiltonian is given by Eq. (4). In the qubit formulation, the non-Abelian charges defined in Eq. (A3) read

$$\hat{Q}_n^1 = \frac{(-1)^n}{2}(\hat{\sigma}_{3n-2}^+\hat{\sigma}_{3n-1}^- + \text{H.c.}), \tag{A5}$$

$$\hat{Q}_n^2 = \frac{i(-1)^n}{2}(\hat{\sigma}_{3n-1}^+\hat{\sigma}_{3n-2}^- - \text{H.c.}), \tag{A6}$$

$$\hat{Q}_n^3 = \frac{1}{4}(\hat{\sigma}_{3n-2}^z - \hat{\sigma}_{3n-1}^z), \tag{A7}$$

$$\hat{Q}_n^4 = -\frac{1}{2}\big(\hat{\sigma}_{3n-2}^{+}\hat{\sigma}_{3n-1}^{z}\hat{\sigma}_{3n}^{-} + \text{H.c.}\big), \tag{A8}$$

$$\hat{Q}_n^5 = \frac{i}{2}\big(\hat{\sigma}_{3n-2}^{+}\hat{\sigma}_{3n-1}^{z}\hat{\sigma}_{3n}^{-} - \text{H.c.}\big), \tag{A9}$$

$$\hat{Q}_n^6 = \frac{(-1)^n}{2}(\hat{\sigma}_{3n-1}^{+}\hat{\sigma}_{3n}^{-} + \text{H.c.}), \tag{A10}$$

$$\hat{Q}_n^7 = \frac{i(-1)^n}{2}(\hat{\sigma}_{3n}^{+}\hat{\sigma}_{3n-1}^{-} - \text{H.c.}), \tag{A11}$$

$$\hat{Q}_n^8 = \frac{1}{4\sqrt{3}}\big(\hat{\sigma}_{3n-2}^{z} + \hat{\sigma}_{3n-1}^{z} - 2\hat{\sigma}_{3n}^{z}\big). \tag{A12}$$

The color electric field Hamiltonian can be obtained by inserting the qubit expressions for the non-Abelian charges in Eqs. (A5)–(A12) into the color electric term in Eq. (A2). We obtain

$$\begin{aligned}\hat{H}_e = {} & \frac{1}{3}\sum_{n=1}^{N-1}(N-n) \\ & \times \big(3 - \hat{\sigma}_{3n-2}^{z}\hat{\sigma}_{3n-1}^{z} - \hat{\sigma}_{3n-2}^{z}\hat{\sigma}_{3n}^{z} - \hat{\sigma}_{3n-1}^{z}\hat{\sigma}_{3n}^{z}\big) \\ & + \sum_{n=1}^{N-2}\sum_{m=n+1}^{N-1}\Big[(N-m)\big(\hat{\sigma}_{3n-2}^{+}\hat{\sigma}_{3n-1}^{-}\hat{\sigma}_{3m-1}^{+}\hat{\sigma}_{3m-2}^{-} \\ & + \hat{\sigma}_{3n-1}^{+}\hat{\sigma}_{3n}^{-}\hat{\sigma}_{3m-1}^{-}\hat{\sigma}_{3m}^{+} + \text{H.c.}\big)(-1)^{n+m} \\ & + (N-m)\big(\hat{\sigma}_{3n-2}^{+}\hat{\sigma}_{3n-1}^{z}\hat{\sigma}_{3n}^{-}\hat{\sigma}_{3m-2}^{-}\hat{\sigma}_{3m-1}^{z}\hat{\sigma}_{3m}^{+} + \text{H.c.}\big) \\ & - \frac{1}{12}(N-m)\hat{\sigma}_{3m-2}^{z}\big(\hat{\sigma}_{3n-1}^{z} + \hat{\sigma}_{3n}^{z} - 2\hat{\sigma}_{3n-2}^{z}\big) \\ & - \frac{1}{12}(N-m)\hat{\sigma}_{3m-1}^{z}\big(\hat{\sigma}_{3n}^{z} + \hat{\sigma}_{3n-2}^{z} - 2\hat{\sigma}_{3n-1}^{z}\big) \\ & - \frac{1}{12}(N-m)\hat{\sigma}_{3m}^{z}\big(\hat{\sigma}_{3n-2}^{z} + \hat{\sigma}_{3n-1}^{z} - 2\hat{\sigma}_{3n}^{z}\big)\Big],\end{aligned} \tag{A13}$$

which exhibits long-range spin-spin interaction as a direct consequence of the gauge elimination. The baryon number operator is proportional to the total magnetization of the system in the qubit encoding

$$\hat{B} = \frac{1}{6}\sum_{n=1}^{3N}\hat{\sigma}_n^z. \tag{A14}$$

2. Hamiltonian for $N = 2$ and reduction to three qubits

We are interested in a basic building block consisting of $N = 2$ lattice sites. The model is then described by a chain with six qubits. The terms in the Hamiltonian read

$$\hat{H}_{\text{kin}} = -\tfrac{1}{2}\big(\hat{\sigma}_1^{+}\hat{\sigma}_2^{z}\hat{\sigma}_3^{z}\hat{\sigma}_4^{-} - \hat{\sigma}_2^{+}\hat{\sigma}_3^{z}\hat{\sigma}_4^{z}\hat{\sigma}_5^{-} + \hat{\sigma}_3^{+}\hat{\sigma}_4^{z}\hat{\sigma}_5^{z}\hat{\sigma}_6^{-} + \text{H.c.}\big), \tag{A15}$$

$$\hat{H}_m = \tfrac{1}{2}\big(6 - \hat{\sigma}_1^z - \hat{\sigma}_2^z - \hat{\sigma}_3^z + \hat{\sigma}_4^z + \hat{\sigma}_5^z + \hat{\sigma}_6^z\big), \tag{A16}$$

$$\hat{H}_e = \tfrac{1}{3}\big(3 - \hat{\sigma}_1^z\hat{\sigma}_2^z - \hat{\sigma}_1^z\hat{\sigma}_3^z - \hat{\sigma}_2^z\hat{\sigma}_3^z\big). \tag{A17}$$

In the sector with baryon number $B = 0$ (i.e., with zero matter-antimatter imbalance), the three terms composing the Hamiltonian commute with the following operator:

$$\hat{CP} = \prod_{n=1}^{3}\hat{\sigma}_n^x\hat{\sigma}_{7-n}^x\hat{W}_{n,7-n}, \tag{A18}$$

where $\hat{W}_{n,n'}$ is the SWAP unitary operator between qubits n and n'. This symmetry corresponds to the composition of a spatial reflection ($\hat{P}$) with respect to the middle of the chain followed by a charge conjugation operation ($\hat{C}$) which flips the spins. Local spin operators $\hat{\sigma}_n^a$ transform as $(\hat{CP})^{\dagger}\hat{\sigma}_n^a\hat{CP} = (\hat{\sigma}^x\hat{\sigma}^a\hat{\sigma}^x)_{7-n}$ under the $\hat{CP}$ operation with $a = x, y, z$ and $n = 1, 2, \dots, 6$. It is thus clear that a convenient basis is the one spanned by states of the form $|\Psi\rangle = \sum_{ijk} c_{ijk}|i\rangle_1|j\rangle_2|k\rangle_3 \otimes \hat{\sigma}_4^x\hat{\sigma}_5^x\hat{\sigma}_6^x|i\rangle_4|j\rangle_5|k\rangle_6$, which are invariant under the $\hat{CP}$ operation and are $B = 0$ eigenstates. Working with this basis, the state of the last three qubits is determined by the state of the first three. As a direct consequence, we can encode the states by using only the first three qubits (i.e., the state of the antimatter) rather than six. The reduced three-qubit Hamiltonian reads

$$\hat{H}_{\text{kin}}^{(3)} = -\tfrac{1}{2}\big(\hat{\sigma}_1^x\hat{\sigma}_2^z\hat{\sigma}_3^z + \hat{\sigma}_1^z\hat{\sigma}_2^x\hat{\sigma}_3^z + \hat{\sigma}_1^z\hat{\sigma}_2^z\hat{\sigma}_3^x\big), \tag{A19}$$

$$\hat{H}_m^{(3)} = 3 - \hat{\sigma}_1^z - \hat{\sigma}_2^z - \hat{\sigma}_3^z, \tag{A20}$$

$$\hat{H}_e^{(3)} = \tfrac{1}{3}\big(3 - \hat{\sigma}_1^z\hat{\sigma}_2^z - \hat{\sigma}_1^z\hat{\sigma}_3^z - \hat{\sigma}_2^z\hat{\sigma}_3^z\big), \tag{A21}$$

and the time evolution is obtained using the Hamiltonian

$$\hat{H}^{(3)} = \hat{H}_{\text{kin}}^{(3)} + \tilde{m}\hat{H}_m^{(3)} + \frac{1}{2x}\hat{H}_e^{(3)}. \tag{A22}$$

3. Inclusion of static charges

Static charges can be effectively incorporated in our model using two flavors of quarks. We use light quarks with mass $\tilde{m}$ for the dynamical charges and heavy quarks with mass $\tilde{M} \gg \tilde{m}$ to represent the external static charges. By definition, the static charges do not enter into the kinetic term, and for simplicity, we remove their contribution from the mass Hamiltonian by a shift in the zero energy definition. The Gauss law must be modified in order to take the color electric field created by the static charges into account: the non-Abelian charges appearing in the color electric Hamiltonian in Eq. (5) are replaced by $\hat{\tilde{\mathbf{Q}}}_n = \hat{\mathbf{Q}}_n^L + \hat{\mathbf{Q}}_n^H$, where $\hat{\mathbf{Q}}_n^L$ are the light dynamical charges defined in Eq. (A3) and $\hat{\mathbf{Q}}_n^H$ is the heavy static source distribution at cell n. We choose the following configuration for the external charges: We place one static anticharge at cell n_1 (odd cell) and a static charge at cell n_2 (even cell). The static charge distribution is thus given by $\hat{\mathbf{Q}}_n^H = \hat{\mathbf{q}}_{n_1}\delta_{n,n_1} + \hat{\mathbf{q}}_{n_2}\delta_{n,n_2}$, where $\hat{q}_n^a = \sum_{i,j=1}^{3}\hat{\eta}_n^{i\dagger}(T^a)_{ij}\hat{\eta}_n^j$ and $\hat{\eta}_n$ are the three color component fermion fields associated with the static charges. Expanding the square in the color electric field Hamiltonian $\hat{H}_e^{(q)} = \sum_{n=1}^{N-1}(\sum_{m\leqslant n}\hat{\tilde{\mathbf{Q}}}_m)^2$, we find that the color electric field Hamiltonian in the presence of external charges $\hat{H}_e^{(q)}$ is the sum of three contributions

$$\hat{H}_e^{(q)} = \hat{H}_e^{(q=0)} + \hat{H}_e^{(qq)} + \hat{H}_e^{(qQ)}, \tag{A23}$$

where $\hat{H}_e^{(q=0)}$ is the color electric field generated by the light dynamical charges alone and is given by Eq. (5), the second term

$$\begin{aligned}\hat{H}_e^{(qq)} = \sum_{a=1}^{8}\big[&\big(\hat{q}_{n_1}^a\big)^2(N-n_1) + \big(\hat{q}_{n_2}^a\big)^2(N-n_2) \\ & + 2\hat{q}_{n_1}^a\hat{q}_{n_2}^a(N-n_2)\big],\end{aligned} \tag{A24}$$

describes the interaction between the two external charges (we assume $n_1 < n_2$ without loss of generality), and

$$\hat{H}_e^{(qQ)} = 2\sum_{a=1}^{8}\sum_{n=1}^{N-1} \hat{Q}_n^a\big[\hat{q}_{n_1}^a(N - \max(n_1, n)) + \hat{q}_{n_2}^a(N - \max(n_2, n))\big] \tag{A25}$$

is the interaction between the external and the dynamical charges. In order to describe the system in terms of qubits, we follow the same steps as before using $3N$ qubits to describe the dynamical charges and adding six extra qubits at the end of the chain to describe the external charges degrees of freedom [see Fig. 4(a)]. For the expression of the external charges in terms of qubits, we can use the definition equations (A5)–(A12) with $n = N + 1$ for $\hat{q}_{n_1}^a$ and $n = N + 2$ for $\hat{q}_{n_2}^a$. In total, we thus need $3N + 6$ qubits to describe the system with two external charges.

4. Trotter Hamiltonian to study pentaquarks

To study the properties of pentaquark states, consisting of four quarks and one antiquark, we consider the minimal system size which can host such a state. We therefore work with $N = 2$ for the light dynamical charges, one static anticharge at site $n_1 = 1$, and one static charge at site $n_2 = 2$. We arrange the light and heavy quarks in the unit cell containing 12 qubits as shown in Fig. 4(a), with the first six qubits describing the light dynamical quarks and the last six qubits encoding the state of the heavy quarks. We define the total baryon number $\hat{B} = \hat{B}_L + \hat{B}_H$ of the system as the sum of the light quark baryon number $\hat{B}_L$ and the heavy quark baryon number $\hat{B}_H$,

$$\hat{B}_L = \frac{1}{6}\sum_{n=1}^{3N} \hat{\sigma}_n^z, \tag{A26}$$

$$\hat{B}_H = \frac{1}{6}\sum_{n=3N+1}^{3N+6} \hat{\sigma}_n^z. \tag{A27}$$

Since we are interested in a pentaquark state, we restrict ourselves to the sector with total baryon number $B = 1$. We choose to study a pentaquark state that contains a heavy diquark. This choice of pentaquark translates into two constraints. First, the absence of anticharge colors on the heavy antiquark sites encoded in qubits 7, 8, and 9 translates into fixing these spins in the vacuum state for this part of the lattice $|\text{vac}\rangle = |\uparrow_7\uparrow_8\uparrow_9\rangle$. Second, imposing that the heavy quark matter sites (encoded in qubits 10, 11, and 12) represent a diquark state requires the last three qubits (qubits 10, 11, and 12) to be in a state with total cell magnetization $M = 1$.

We perform a time evolution experiment starting from the baryon state (consisting of one light quark and one heavy diquark) which reads in spin formulation

$$\begin{aligned}|\Psi_B\rangle = &\frac{1}{\sqrt{3}}(|\uparrow\uparrow\uparrow\uparrow\downarrow\downarrow\rangle_L\,|\uparrow\uparrow\uparrow\downarrow\uparrow\uparrow\rangle_H \\ &- |\uparrow\uparrow\uparrow\downarrow\uparrow\downarrow\rangle_L\,|\uparrow\uparrow\uparrow\uparrow\downarrow\uparrow\rangle_H \\ &- |\uparrow\uparrow\uparrow\downarrow\downarrow\uparrow\rangle_L\,|\uparrow\uparrow\uparrow\uparrow\uparrow\downarrow\rangle_H),\end{aligned} \tag{A28}$$

where the first ket with subscript L represents the light quarks while the second one with subscript H encodes the heavy quarks. It is instructive to show how this combination is obtained. This superposition of three basis kets is the only one with three particles satisfying the constraint of total baryon number $B = 1$ and local (light and heavy) baryon number conservation as explained above. This state is an eigenstate of the electric field Hamiltonian equation (A40). Since the electric field Hamiltonian is diagonal, any normalized linear combination of these three basis states could in principle represent a convenient strong coupling eigenstate. However, the eigenstates are also constrained by the fact that their total non-Abelian charges must vanish (we are working with color-neutral objects):

$$\hat{\mathbf{Q}}_{\text{tot}}^a\,|\Psi_B\rangle = \sum_{n=1}^{N+2}\hat{Q}_n^a\,|\Psi_B\rangle = 0, \tag{A29}$$

for $a = 1, 2, \ldots, 8$. Using the expression of the non-Abelian charges in Eqs. (A5)–(A12), we can verify that the combination in Eq. (A28) is indeed a color-neutral object. For the charges in the Cartan subalgebra, i.e., the one generated by the diagonal Gell-Mann matrices, Q_n^3 and Q_n^8 [see Eqs. (A7) and (A12)], the verification is straightforward. The verification for the nondiagonal charges is not difficult, and we will detail out as an example the calculation for $a = 1$ [Eq. (A5)]. We first write the superposition as

$$|\Psi_B\rangle = \frac{1}{\sqrt{3}}(|1\rangle - |2\rangle - |3\rangle) \tag{A30}$$

with

$$|1\rangle = |\uparrow\uparrow\uparrow\uparrow\downarrow\downarrow\rangle_L\,|\uparrow\uparrow\uparrow\downarrow\uparrow\uparrow\rangle_H\,, \tag{A31}$$

$$|2\rangle = |\uparrow\uparrow\uparrow\downarrow\uparrow\downarrow\rangle_L\,|\uparrow\uparrow\uparrow\uparrow\downarrow\uparrow\rangle_H\,, \tag{A32}$$

$$|3\rangle = |\uparrow\uparrow\uparrow\downarrow\downarrow\uparrow\rangle_L\,|\uparrow\uparrow\uparrow\uparrow\uparrow\downarrow\rangle_H\,. \tag{A33}$$

Let us now write the action of

$$Q_{\text{tot}}^1 = \sum_{n=1}^{N+2}\frac{(-1)^n}{2}(\sigma_{3n-2}^+\sigma_{3n-1}^- + \text{H.c.})$$

on the three basis states. From the expression of the charge, it is clear that it acts on the first two spins of each cell and it has a nonzero effect only if they are in opposite directions. In terms of particles, the charge Q_{tot}^1 generates a tunneling between red and green particles whenever one site is occupied and its neighboring site is empty. We have

$$\begin{aligned}Q_{\text{tot}}^1\,|1\rangle = &\tfrac{1}{2}(|\uparrow\uparrow\uparrow\downarrow\uparrow\downarrow\rangle_L\,|\uparrow\uparrow\uparrow\downarrow\uparrow\uparrow\rangle_H \\ &+ |\uparrow\uparrow\uparrow\uparrow\downarrow\downarrow\rangle_L\,|\uparrow\uparrow\uparrow\uparrow\downarrow\uparrow\rangle_H),\end{aligned} \tag{A34}$$

$$\begin{aligned}Q_{\text{tot}}^1\,|2\rangle = &\tfrac{1}{2}(|\uparrow\uparrow\uparrow\uparrow\downarrow\downarrow\rangle_L\,|\uparrow\uparrow\uparrow\uparrow\downarrow\uparrow\rangle_H \\ &+ |\uparrow\uparrow\uparrow\downarrow\uparrow\downarrow\rangle_L\,|\uparrow\uparrow\uparrow\downarrow\uparrow\uparrow\rangle_H),\end{aligned} \tag{A35}$$

$$Q_{\text{tot}}^1\,|3\rangle = 0. \tag{A36}$$

This shows that $|1\rangle$ and $|2\rangle$ must come with opposite signs in the superposition in order to have $Q_{\text{tot}}^1\,|\Psi_B\rangle = 0$. Similarly, the constraints on the remaining charges impose that the ket $|3\rangle$ must come with a sign opposite to the one of the basis state $|1\rangle$, which leads to the superposition in Eq. (A28).

Note that the state of the first three qubits in the heavy quark ket is fixed (due to the absence of heavy anticharges) and the state of the last three qubits in the heavy quark ket corresponds to the flipped version of the last three qubits in the light quark ket. As a consequence, the heavy quark sites do not need to be included in the quantum simulation. This is also reflected in the Hamiltonian governing the dynamics, which is given in Eqs. (A15)–(A17) and involves only the first six qubits.

Since the state of the light quarks is sufficient to reconstruct the full state of the system, we rewrite the baryon initial state in terms of the light quark ket only:

$$|\Psi_B\rangle = \frac{1}{\sqrt{3}}(|\uparrow\uparrow\uparrow\uparrow\downarrow\downarrow\rangle_L - |\uparrow\uparrow\uparrow\downarrow\uparrow\downarrow\rangle_L - |\uparrow\uparrow\uparrow\downarrow\downarrow\uparrow\rangle_L). \tag{A37}$$

Each of the three terms in the superposition corresponds to a different color sector. The first ket has a light redness number $\hat{\mathcal{R}}_L = (\hat{\sigma}_1^z + \hat{\sigma}_4^z)/2$ equal to 1. Similarly, the second ket in the expansion has a light greenness number $\hat{\mathcal{G}}_L = (\hat{\sigma}_2^z + \hat{\sigma}_5^z)/2$ equal to 1, while the last term has a light blueness number defined as $\hat{\mathcal{B}}_L = (\hat{\sigma}_3^z + \hat{\sigma}_6^z)/2$ equal to 1. Since the Hamiltonian in Eqs. (A15)–(A17) preserves the light redness, greenness, and blueness quantum numbers, the time evolution will not mix the different color sectors. As a consequence, it is sufficient to time-evolve only one of the kets in Eq. (A37) rather than applying the time evolution operator to the superposition. This observation allows us to significantly decrease the complexity of our Trotter protocol. We thus use $|\Psi_B^{(r)}\rangle = |\uparrow\uparrow\uparrow\uparrow\downarrow\downarrow\rangle_L$ as our initial state, where the superscript indicates that this state belongs to the red sector. Furthermore, since qubit 1 and qubit 4 are not affected by the time evolution, the dynamics is effectively governed by the four-qubit Hamiltonian $\hat{H}^{(4)} = \hat{H}^{(4)}_{\text{kin}} + (1/2x)\hat{H}^{(4)}_e + \tilde{m}\hat{H}^{(4)}_m$ with

$$\hat{H}^{(4)}_{\text{kin}} = -\tfrac{1}{2}\big(-\hat{\sigma}_2^+\hat{\sigma}_3^z\hat{\sigma}_5^- + \hat{\sigma}_3^+\hat{\sigma}_5^z\hat{\sigma}_6^- + \text{H.c.}\big), \tag{A38}$$

$$\hat{H}^{(4)}_m = \tfrac{1}{2}\big(6 - \hat{\sigma}_2^z - \hat{\sigma}_3^z + \hat{\sigma}_5^z + \hat{\sigma}_6^z\big), \tag{A39}$$

$$\hat{H}^{(4)}_e = \tfrac{1}{3}\big(3 - \hat{\sigma}_2^z - \hat{\sigma}_3^z - \hat{\sigma}_2^z\hat{\sigma}_3^z\big). \tag{A40}$$

We find that a Trotter step time evolution of the four-qubit Hamiltonian can be realized using 18 CNOT gates. In our time evolution experiments (see Fig. 4), we measure the total particle number of the time-evolved state $|\Psi(t)\rangle = e^{-it\hat{H}}|\Psi_B\rangle$,

$$\begin{aligned}\langle\hat{\mathcal{N}}(t)\rangle &= \langle\Psi(t)|\,\hat{H}_m\,|\Psi(t)\rangle + 2\\ &= \langle\Psi^{(r)}(t)|\,\hat{H}^{(4)}_m\,|\Psi^{(r)}(t)\rangle + 3,\end{aligned} \tag{A41}$$

where $|\Psi^{(r)}(t)\rangle = e^{-it\hat{H}^{(4)}}|\Psi_B^{(r)}\rangle$ is the time-evolved state within the red sector.

APPENDIX B: EXPERIMENTAL DETAILS

1. Trotter evolution

In this section, we provide the circuit implementing one Trotter step for the tetraquark experiments. Although the Hamiltonian of Eqs. (A19)–(A21) is expressed in terms of Pauli X and Z gates, a simple rotation to Y and Z gates allows for more cancellations among CNOT gates. This is especially valuable on hardware that does not provide all-to-all connectivity among the qubits. The first half of our first-order Trotter step is displayed in Fig. 6, and to match the available hardware, it does not use any entangling gates directly between q_1 and q_3. The second half of the Trotter step is the same except for a relabeling of $q_1 \leftrightarrow q_3$.

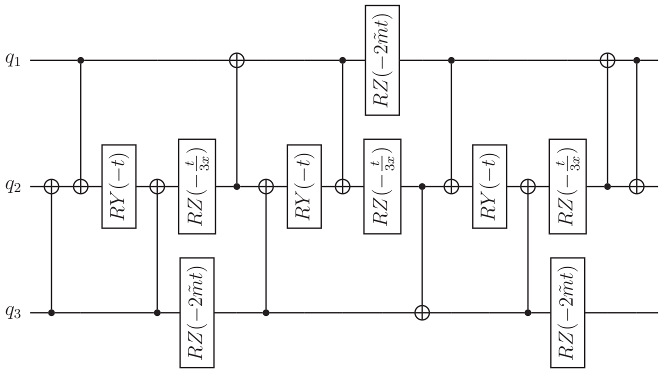

FIG. 6. The first half of a Trotter step is shown in this figure. The second half is identical except for the interchange of two qubits: $q_1 \leftrightarrow q_3$. Note that a pair of CNOT gates can be canceled where the two halves meet.

Let us provide details about the procedure to obtain the Trotter circuit in Fig. 6. We start from the three-qubit Hamiltonian in Eqs. (A19)–(A21) and perform a rotation to transform the X Pauli matrices into Y Pauli matrices. The unitary operator realizing this rotation is given by

$$\hat{U} = \exp\left(i\frac{\pi}{2}(Z_1 + Z_2 + Z_3)\right) \tag{B1}$$

and transforms the three-qubit Hamiltonian into

$$\hat{H}_{\text{kin}} = -\tfrac{1}{2}(Y_1Z_2Z_3 + Z_1Y_2Z_3 + Z_1Z_2Y_3), \tag{B2}$$

$$\hat{H}_m = 3 - Z_1 - Z_2 - Z_3, \tag{B3}$$

$$\hat{H}_e = \tfrac{1}{3}(3 - Z_1Z_2 - Z_1Z_3 - Z_2Z_3). \tag{B4}$$

Note that the mass term and electric term are not affected by the rotation as they only depend on Z Pauli operators. Taking the time evolution operator of each term in the Hamiltonian, we see that a first-order Trotterization produces terms of the form

$$\exp\left(i\frac{t}{2}Z_1Y_2Z_3\right), \quad \exp\left(i\frac{t}{6x}Z_1Z_2\right), \tag{B5}$$

which can be implemented using the following identities:

$$\exp(i\theta Z_1Y_2Z_3) = \text{CX}_{12}\text{CX}_{32}\text{RY}_2(-2\theta)\text{CX}_{32}\text{CX}_{12} \tag{B6}$$

and

$$\exp(i\theta Z_1Z_2) = \text{CX}_{12}\text{RZ}_2(-2\theta)\text{CX}_{12}, \tag{B7}$$

where CX_{ij} is a CNOT gate with control on qubit i and target on qubit j and $\text{RZ}_j(\theta) = e^{-i\theta/2Z_j}$ and $\text{RY}_j(\theta) = e^{-i\theta/2Y_j}$ are the usual single qubit rotation gates. By defining

$$U_{ijk} = e^{it/2Z_iY_jZ_k}e^{it\tilde{m}Z_k}e^{it/6xZ_iZ_j} \tag{B8}$$

and using the identities above, the circuit can be obtained by implementing the following unitary operation:

$$U_{\text{Trotter}} = U_{123}U_{312}U_{231}. \tag{B9}$$

The error of our first-order Trotter scheme $\hat{U}_T(t)$ of the true evolution induced by $\hat{H} = \sum_j \hat{h}_j$ can be estimated employing the relation (with spectral norm) [66]

$$||\hat{U}_T(t) - \mathrm{e}^{-it\hat{H}}|| = O(\alpha t^2). \tag{B10}$$

Here, the $\hat{h}_j$ are specified by the components of the qubit Hamiltonians and

$$\alpha = \sum_{j,k} ||[\hat{h}_j, \hat{h}_k]||. \tag{B11}$$

When applying n Trotter steps, the total error of that evolution is then given as

$$\left\|\hat{U}_T^n(t/n) - \mathrm{e}^{-it\hat{H}}\right\| = O\left(\frac{\alpha^2 t^2}{n}\right). \tag{B12}$$

For the cases examined in this paper, we find that

$$\alpha_{\text{tetra}} = 8|\tilde{m}| + \frac{8}{3|x|}, \tag{B13}$$

$$\alpha_{\text{penta}} = 2 + \alpha_{\text{tetra}}, \tag{B14}$$

employing Eqs. (A19)–(A21) and Eqs. (A38)–(A40), respectively.

2. Scalability and resource estimation

The experiments carried out were done for the minimal number of sites $N = 2$, to be implemented on current quantum computers. Here we estimate the number of CNOT gates needed to implement time evolution for larger system sizes N. For simplicity, we assume here all-to-all connectivity for the quantum hardware, as available in trapped-ion quantum computers, and estimate the number of CNOT operations required to simulate one Trotter step for N lattice sites (corresponding to $3N$ qubits). Consider a Pauli string $\hat{P} = \hat{P}_1\hat{P}_2\cdots\hat{P}_m$ of length m with $\hat{P}_i = \{X, Y, Z\}$. The unitary $e^{-it\hat{P}}$ can be implemented using $2(m-1)$ CNOT gates. This allows us to estimate the number of CNOT operations by counting the number of Pauli strings and their length in each term of the Hamiltonian in Eq. (2). The kinetic term in Eq. (3) has $3(N-1)$ terms of the form $\hat{\sigma}^+\hat{\sigma}^z\hat{\sigma}^z\hat{\sigma}^- + \text{H.c.}$, which corresponds to two Pauli strings $XZZX$ and $YZZY$ of length 4. Thus $36(N-1)$ CNOT gates are needed to implement one Trotter step for the kinetic term. The mass Hamiltonian in Eq. (4) can be implemented using only Z rotations and does not necessitate the use of entangling gates. The color electric Hamiltonian in Eq. (A13) is the most costly in terms of entangling gates as it involves a number of terms growing quadratically with the size of the system N. The first term in Eq. (A13) has $3(N-1)$ Pauli strings of the form ZZ, which amounts to $6(N-1)$ CNOT gates. The double sum also involves ZZ terms, of which there are $9(N^2-3N+2)/2$, therefore contributing with $9(N^2-3N+2)$ CNOT gates. The four-body term $\hat{\sigma}^+\hat{\sigma}^-\hat{\sigma}^+\hat{\sigma}^-$ generates nine Pauli strings of length 4 $(XXXX, XYXX, XXYY, \dots)$; thus we need $54(N^2-3N+2)$ CNOT gates to simulate such a term. Finally, the six-body term $\hat{\sigma}^+\hat{\sigma}^z\hat{\sigma}^-\hat{\sigma}^-\hat{\sigma}^z\hat{\sigma}^+$ can be decomposed into eight Pauli strings of length 6 and can be implemented using $40(N^2-3N+2)$ CNOT gates. In total, we thus find that the number of CNOT gates needed to implement one Trotter step of time evolution under the qubit Hamiltonian in Eq. (2) is given by $103N^2 - 267N + 164$ and grows at most quadratically in the number of lattice sites N.

The general formalism developed presents a promising approach for studying larger system as the qubit encoding is naturally scalable to larger lattice volumes. Additionally, the number of CNOT gates necessary to simulate the dynamics of the encoded Hamiltonian grows quadratically and not exponentially in the number of qubits. It is also worth noting that the SU(3) model studied here, which involves the gauge group of QCD, is significantly more complex than the U(1) model studied in Refs. [35,67]. This increased complexity translates to a larger gate depth, with up to 80 CNOT gates being used, surpassing the number of CNOT gates used in the previous studies.

As gate depth increases, the need for error correction techniques may become more crucial, transitioning from error mitigation to error correction strategies. Future quantum computers are anticipated to have larger qubit registers and incorporate error correction methods, although these approaches are still considered works in progress, and different platforms have their own road maps (depending on the underlying hardware and architecture) for achieving scalability.

3. Quantum hardware and error mitigation

In the main text we noted that the experiments have been carried out on various quantum computers in the IBM lineup. Table I contains excerpts of the calibration taken by IBM during the time of our calculations. Note that CNOT gates take around 300 to 500 ns and hence for 80 CNOT gates the execution length is on the order of 40 μs, which is faster than any of the measured coherence times for the qubits used in the experiments.

As described in the main text, we apply the randomized compiling techniques as described in Ref. [20] to reduce errors introduced by imperfect CNOT gates. Here, we perform an average over different executions of the same base circuit, where each CNOT operation $\hat{U}_{cx}$ is replaced by $\hat{U}_r\hat{U}_{cx}\hat{U}_r^\dagger$, where $\hat{U}_r$ is a basis transformation that, in an ideal setting, would not alter the action of the CNOT gate. The $\hat{U}_r$ are randomly chosen from a list of 16 possibilities (see Ref. [20] for the full list). The averaging then transforms any coherent gate errors into incoherent ones, which can be equivalently understood as the random unitary model of quantum decoherence, where decoherence is introduced via a classical, randomly fluctuating field.

We perform two kinds of Trotter evolution circuits on the hardware. We first perform a physical run, which aims to evolve the state up to the final time $t = t_f$, and then a second mitigation circuit evolves the state up to $t = t'$ and back to $t = 0$. For Trotter steps where $N_{\text{T}}/2$ is even, we have $t' = t_f/2$. Since our circuit always applies two Trotter steps at once, for $N_{\text{T}} = 2$ (6) we have $t' = t_f$ ($\frac{4}{3}t_f$), and the mitigation circuit contains more CNOT gates than the physical circuit, which we have to correct for. During the experiment, we alternate

TABLE I. Excerpts from the calibration of the superconducting qubits employed by IBM around the time of tetraquark experiments 1 and 2 (first three rows), and the last experiment examining the pentaquark (last row).

System name	Qubits	T_1 (μs)				T_2 (μs)				Largest Pauli error	Largest CNOT error
ibmq_lima	0, 1, 2	106.58	59.93	153.32		180.56	139.9	161.82		1.962×10^{-4}	5.237×10^{-3}
ibm_geneva	24, 25, 26	305.17	353.86	444.63		358.17	197.83	392.43		9.966×10^{-4}	7.725×10^{-3}
ibm_peekskill	22, 24, 25	342.00	269.12	161.79		335.64	333.85	418.65		1.192×10^{-4}	4.417×10^{-3}
ibmq_lima	0, 1, 3, 4	106.58	59.93	106.47	23.72	180.56	139.9	99.2	30.62	6.403×10^{-4}	1.602×10^{-2}

between physical and mitigation circuits to avoid any biases that could be caused by slow drifts in the experimental setting. We then correct the expectation value of an observable $\hat{O}$ by comparing its measured value for the physical circuits (index "phys, meas") and the measured value for the mitigation circuits (index "mitig, meas") as

$$\langle\hat{O}\rangle_{\text{phys, true}} = \left(\frac{\langle\hat{O}\rangle_{\text{mitig, true}}}{\langle\hat{O}\rangle_{\text{mitig, meas}}}\right)^{\kappa} \langle\hat{O}\rangle_{\text{phys, meas}}, \qquad \text{(B15)}$$

where κ is the ratio of the number of CNOT gates in the physical and the mitigation circuits. Note that $\langle\hat{O}\rangle_{\text{mitig, true}}$ is known, since it is given through the state at $t = 0$ which is the initial state.

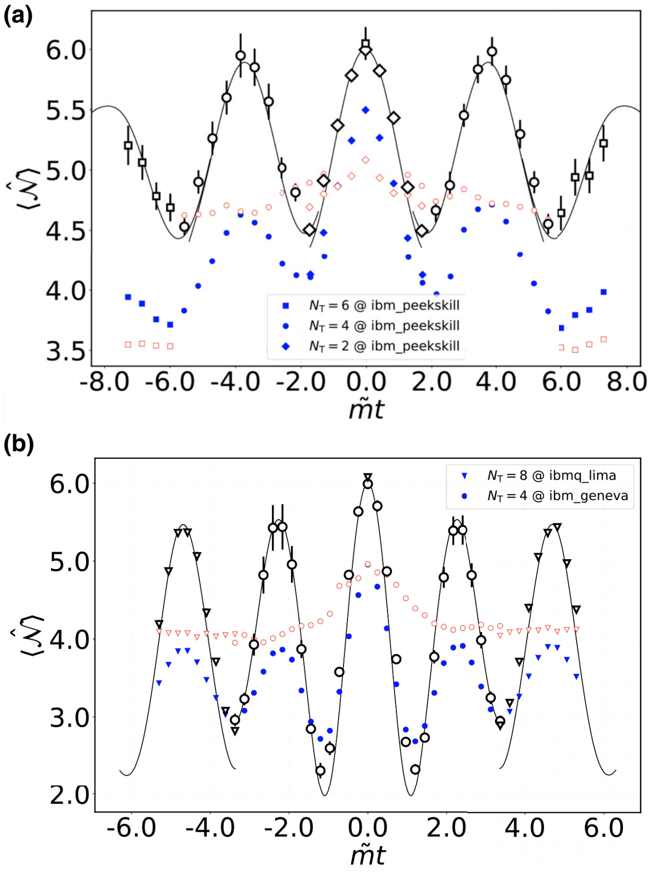

FIG. 7. (a) Experimental results for $\tilde{m} = 1.2$ and $x = 0.8$. The mitigated data (large symbols with error bars) have already been shown in the main text. The solid blue symbols correspond to the physical runs, while the open red symbols are the results of the mitigation runs. The shape of the symbols denotes the number of Trotter steps and the specific IBM machine that was employed (see main text). (b) The equivalent data for the case $\tilde{m} = 0.45$.

In Fig. 7 we show the collected data that have been used to produce Fig. 3 of the main text. The physical runs are shown in blue, while the corresponding mitigation runs are shown in red, with the symbols according to the mitigated data. Note that for $N_\mathrm{T} \in \{2, 6\}$ we have $\kappa = \frac{1}{2}$ and $\kappa = 1$ otherwise. Furthermore, the mitigation has been performed on the observable $\hat{H}_m^{(3)} - 3 = -(\hat{Z}_1 + \hat{Z}_2 + \hat{Z}_3)$. For Fig. 8 we have $\kappa = 1$ and mitigated $\hat{H}_m^{(4)} - 3$.

4. Bayesian inference analysis

We model the obtained data D as draws from a normal distribution with variance σ, where the mean S_K is given by a cosine series

$$S_K = \sum_i^K A_i \cos(\omega_i t + \phi_i) + \xi, \qquad \text{(B16)}$$

with uniform priors on the frequencies ω_i and the amplitudes A_i, while the priors for the phases ϕ_i and the offset ξ are normal distributions located at zero. The uniform priors are adjusted to include the frequencies that are visible from the data by eye. The prior on σ is given by the maximum of 0.3 and the value of the largest error bar in the data set. Note that each data set stemming from different N_T is modeled as a separate likelihood while the parameters are shared. After obtaining a representation of the posterior distribution for the parameters $\theta = \{A_i, \omega_i, \phi_i, \xi, \sigma\}$, $P(\theta|D)$, via Monte Carlo sampling from Bayes's rule [33], we sample the posterior predictive distribution $P(D'|D) = \int_\Theta P(\Theta = \theta|D)P(D'|\Theta = \theta)$,

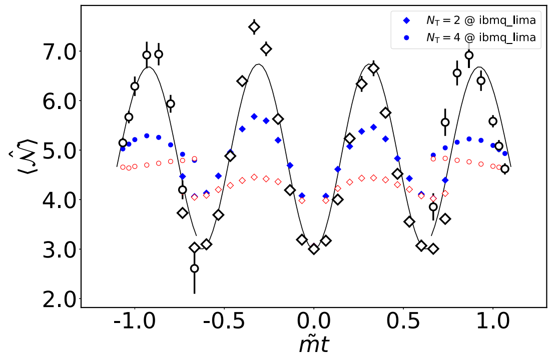

FIG. 8. Experimental results for the pentaquark, for $\tilde{m} = 0.1$ and $x = 3.0$. As in Fig. 7, the solid blue symbols mark the physical runs, while the open red symbols correspond to the mitigation runs. As before, the shape of the symbols denotes the number of Trotter steps and the specific IBM machine that was employed.

TABLE II. Bayesian point estimates and HDI for the two tetraquark experiments, where $x = 0.8$ and $\tilde{m} = 1.2$ or $\tilde{m} = 0.45$, respectively.

	$\tilde{m} = 1.2$		$\tilde{m} = 0.45$	
	Point estimate	HDI	Point estimate	HDI
A_1	0.689	[0.582, 0.752]	0.622	[0.252, 1.560]
A_2	−0.0135	[−0.014, 0.122]	1.182	[0.352, 1.606]
$\omega_1/(2\pi)$	0.262	[0.254, 0.267]	0.482	[0.409, 0.545]
$\omega_2/(2\pi)$	0.338	[0.000, 0.712]	0.427	[0.297, 0.502]
ϕ_1	−0.045	[−0.102, 0.020]	0.009	[−0.114, 0.186]
ϕ_2	−0.549	[−3.425, 2.724]	−0.025	[−0.083, 0.032]
ξ	5.243	[5.127, 5.304]	4.220	[4.135, 4.299]
σ_2	0.056	[0.026, 0.091]		
σ_4	0.087	[0.047, 0.130]	0.226	[0.083, 0.315]
σ_6	0.340	[0.208, 0.461]		
σ_8			0.145	[0.038, 0.432]

where Θ denotes the collective random variables for all parameters. The values for the point estimates and HDI for all parameters can be found in Table II. Note that in both cases we chose $K = 2$. For $\tilde{m} = 1.2$, the low amplitude of the second frequency demonstrates well that the dynamics are indeed dominated by the transition of the baryon-antibaryon and the tetraquark state, while we find two competing frequencies in the case $\tilde{m} = 0.45$. Furthermore, we note that in the latter case, the highest density intervals (HDIs) of the frequencies are not overlapping, while the HDI for ω_2 in the $\tilde{m} = 1.2$ case spans a wide range, indicating that the single frequency ω_1 is mostly enough to describe the whole recorded signal.

[1] H.-X. Chen, W. Chen, X. Liu, Y.-R. Liu, and S.-L. Zhu, An updated review of the new hadron states, Rep. Prog. Phys. **86**, 026201 (2023).

[2] M. C. Bañuls, R. Blatt, J. Catani, A. Celi, J. I. Cirac, M. Dalmonte, L. Fallani, K. Jansen, M. Lewenstein, S. Montangero, C. A. Muschik, B. Reznik, E. Rico, L. Tagliacozzo, K. Van Acoleyen, F. Verstraete, U.-J. Wiese, M. Wingate, J. Zakrzewski, and P. Zoller, Simulating lattice gauge theories within quantum technologies, Eur. Phys. J. D **74**, 165 (2020).

[3] Z. Davoudi, C. W. Bauer, A. Balantekin, T. Bhattacharya, M. Carena, W. A. de Jong, P. Draper, A. El-Khadra, N. Gemelke, M. Hanada, D. Kharzeev, H. Lamm, Y.-Y. Li, J. Liu, M. Lukin, Y. Meurice, C. Monroe, B. Nachman, G. Pagano, J. Preskill, E. Rinaldi *et al.*, Quantum simulation for high energy physics, PRX Quantum **4**, 027001 (2023).

[4] M. Dalmonte and S. Montangero, Lattice gauge theory simulations in the quantum information era, Contemp. Phys. **57**, 388 (2016).

[5] P. Silvi, Y. Sauer, F. Tschirsich, and S. Montangero, Tensor network simulation of an SU(3) lattice gauge theory in 1D, Phys. Rev. D **100**, 074512 (2019).

[6] E. A. Martinez, C. A. Muschik, P. Schindler, D. Nigg, A. Erhard, M. Heyl, P. Hauke, M. Dalmonte, T. Monz, P. Zoller, and R. Blatt, Real-time dynamics of lattice gauge theories with a few-qubit quantum computer, Nature (London) **534**, 516 (2016).

[7] N. Klco, E. F. Dumitrescu, A. J. McCaskey, T. D. Morris, R. C. Pooser, M. Sanz, E. Solano, P. Lougovski, and M. J. Savage, Quantum-classical computation of Schwinger model dynamics using quantum computers, Phys. Rev. A **98**, 032331 (2018).

[8] C. Kokail, C. Maier, R. van Bijnen, T. Brydges, M. K. Joshi, P. Jurcevic, C. A. Muschik, P. Silvi, R. Blatt, C. F. Roos, and P. Zoller, Self-verifying variational quantum simulation of lattice models, Nature (London) **569**, 355 (2019).

[9] H.-H. Lu, N. Klco, J. M. Lukens, T. D. Morris, A. Bansal, A. Ekström, G. Hagen, T. Papenbrock, A. M. Weiner, M. J. Savage, and P. Lougovski, Simulations of subatomic many-body physics on a quantum frequency processor, Phys. Rev. A **100**, 012320 (2019).

[10] A. Mil, T. V. Zache, A. Hegde, A. Xia, R. P. Bhatt, M. K. Oberthaler, P. Hauke, J. Berges, and F. Jendrzejewski, A scalable realization of local U(1) gauge invariance in cold atomic mixtures, Science **367**, 1128 (2020).

[11] F. M. Surace, P. P. Mazza, G. Giudici, A. Lerose, A. Gambassi, and M. Dalmonte, Lattice Gauge Theories and String Dynamics in Rydberg Atom Quantum Simulators, Phys. Rev. X **10**, 021041 (2020).

[12] B. Yang, H. Sun, R. Ott, H.-Y. Wang, T. V. Zache, J. C. Halimeh, Z.-S. Yuan, P. Hauke, and J.-W. Pan, Observation of gauge invariance in a 71-site Bose–Hubbard quantum simulator, Nature (London) **587**, 392 (2020).

[13] Z. Zhou, G. Su, J. Halimeh, R. Ott, H. Sun, P. Hauke, B. Yang, Z. Yuan, J. Berges, and J. Pan, Thermalization dynamics of a gauge theory on a quantum simulator, Science **377**, 311 (2022).

[14] N. H. Nguyen, M. C. Tran, Y. Zhu, A. M. Green, C. H. Alderete, Z. Davoudi, and N. M. Linke, Digital quantum simulation of the schwinger model and symmetry protection with trapped ions, PRX Quantum **3**, 020324 (2022).

[15] Y. Y. Atas, J. Zhang, R. Lewis, A. Jahanpour, J. F. Haase, and C. A. Muschik, SU(2) hadrons on a quantum computer via a variational approach, Nat. Commun. **12**, 6499 (2021).

[16] N. Klco, M. J. Savage, and J. R. Stryker, SU(2) non-Abelian gauge field theory in one dimension on digital quantum computers, Phys. Rev. D **101**, 074512 (2020).

[17] S. A. Rahman, R. Lewis, E. Mendicelli, and S. Powell, SU(2) lattice gauge theory on a quantum annealer, Phys. Rev. D **104**, 034501 (2021).

[18] A. Ciavarella, N. Klco, and M. J. Savage, Trailhead for quantum simulation of SU(3) Yang-Mills lattice gauge theory in the local multiplet basis, Phys. Rev. D **103**, 094501 (2021).

[19] M. Illa and M. J. Savage, Basic elements for simulations of standard model physics with quantum annealers: Multigrid and clock states, Phys. Rev. A **106**, 052605 (2022).

[20] S. A. Rahman, R. Lewis, E. Mendicelli, and S. Powell, Self-mitigating Trotter circuits for SU(2) lattice gauge theory on a quantum computer, Phys. Rev. D **106**, 074502 (2022).

[21] M. Fromm, O. Philipsen, and C. Winterowd, Dihedral lattice gauge theories on a quantum annealer, EPJ Quantum Technol. **10**, 31 (2023).

[22] R. C. Farrell, I. A. Chernyshev, S. J. Powell, N. A. Zemlevskiy, M. Illa, and M. J. Savage, Preparations for quantum simulations of quantum chromodynamics in 1+1 dimensions. I. Axial gauge, Phys. Rev. D **107**, 054512 (2023).

[23] R. C. Farrell, I. A. Chernyshev, S. J. Powell, N. A. Zemlevskiy, M. Illa, and M. J. Savage, Preparations for quantum simulations of quantum chromodynamics in 1+ 1 dimensions. II. Single-baryon β-decay in real time, Phys. Rev. D **107**, 054513 (2023).

[24] J. Kogut and L. Susskind, Hamiltonian formulation of Wilson's lattice gauge theories, Phys. Rev. D **11**, 395 (1975).

[25] D. Griffiths, *Introduction to Elementary Particles* (Wiley, New York, 2020).

[26] E. Zohar, J. I. Cirac, and B. Reznik, Quantum simulations of lattice gauge theories using ultracold atoms in optical lattices, Rep. Prog. Phys. **79**, 014401 (2015).

[27] S. Kühn, E. Zohar, J. I. Cirac, and M. C. Bañuls, Non-Abelian string breaking phenomena with matrix product states, J. High Energy Phys. 07 (2015) 130.

[28] P. Jordan and E. Wigner, Über das Paulische Äquivalenzverbot, Z. Phys. **47**, 631 (1928).

[29] B. Efron, Bootstrap methods: Another look at the jackknife, Ann. Stat. **7**, 1 (1979).

[30] S. Lloyd, Universal quantum simulators, Science **273**, 1073 (1996).

[31] A. Hashim, R. K. Naik, A. Morvan, J.-L. Ville, B. Mitchell, J. M. Kreikebaum, M. Davis, E. Smith, C. Iancu, K. P. O'Brien, I. Hincks, J. J. Wallman, J. Emerson, and I. Siddiqi, Randomized Compiling for Scalable Quantum Computing on a Noisy Superconducting Quantum Processor, Phys. Rev. X **11**, 041039 (2021).

[32] IBM Quantum, 2022, https://quantum-computing.ibm.com/.

[33] J. Kruschke, *Doing Bayesian Data Analysis: A Tutorial with R, JAGS, and Stan*, 2nd ed. (Academic, New York, 2014).

[34] C. J. Hamer, Z. Weihong, and J. Oitmaa, Series expansions for the massive Schwinger model in Hamiltonian lattice theory, Phys. Rev. D **56**, 55 (1997).

[35] C. Muschik, M. Heyl, E. Martinez, T. Monz, P. Schindler, B. Vogell, Marcello Dalmonte, P. Hauke, R. Blatt, and P. Zoller, U(1) Wilson lattice gauge theories in digital quantum simulators, New J. Phys. **19**, 103020 (2017).

[36] S. P. Jordan, K. S. M. Lee, and J. Preskill, Quantum algorithms for quantum field theories, Science **336**, 1130 (2012).

[37] S. P. Jordan, K. S. Lee, and J. Preskill, Quantum algorithms for fermionic quantum field theories, arXiv:1404.7115.

[38] Y. Tong, V. V. Albert, J. R. McClean, J. Preskill, and Y. Su, Provably accurate simulation of gauge theories and bosonic systems, Quantum **6**, 816 (2022).

[39] R. Ott, T. V. Zache, F. Jendrzejewski, and J. Berges, Scalable Cold-Atom Quantum Simulator for Two-Dimensional QED, Phys. Rev. Lett. **127**, 130504 (2021).

[40] V. Kasper, F. Hebenstreit, F. Jendrzejewski, M. K. Oberthaler, and J. Berges, Implementing quantum electrodynamics with ultracold atomic systems, New J. Phys. **19**, 023030 (2017).

[41] V. Kasper, F. Hebenstreit, M. K. Oberthaler, and J. Berges, Schwinger pair production with ultracold atoms, Phys. Lett. B **760**, 742 (2016).

[42] B. Andrade, Z. Davoudi, T. Graß, M. Hafezi, G. Pagano, and A. Seif, Engineering an effective three-spin hamiltonian in trapped-ion systems for applications in quantum simulation, Quantum Sci. Technol. **7**, 034001 (2022).

[43] Z. Davoudi, N. M. Linke, and G. Pagano, Toward simulating quantum field theories with controlled phonon-ion dynamics: A hybrid analog-digital approach, Phys. Rev. Res. **3**, 043072 (2021).

[44] L. Tagliacozzo, A. Celi, P. Orland, M. Mitchell, and M. Lewenstein, Simulation of non-Abelian gauge theories with optical lattices, Nat. Commun. **4**, 2615 (2013).

[45] A. Mezzacapo, E. Rico, C. Sabín, I. L. Egusquiza, L. Lamata, and E. Solano, Non-Abelian SU(2) Lattice Gauge Theories in Superconducting Circuits, Phys. Rev. Lett. **115**, 240502 (2015).

[46] J. Bender, E. Zohar, A. Farace, and J. I. Cirac, Digital quantum simulation of lattice gauge theories in three spatial dimensions, New J. Phys. **20**, 093001 (2018).

[47] E. Zohar and J. I. Cirac, Eliminating fermionic matter fields in lattice gauge theories, Phys. Rev. B **98**, 075119 (2018).

[48] T. V. Zache, N. Mueller, J. T. Schneider, F. Jendrzejewski, J. Berges, and P. Hauke, Dynamical Topological Transitions in the Massive Schwinger Model with a θ Term, Phys. Rev. Lett. **122**, 050403 (2019).

[49] V. Kasper, T. V. Zache, F. Jendrzejewski, M. Lewenstein, and E. Zohar, Non–Abelian gauge invariance from dynamical decoupling, Phys. Rev. D **107**, 014506 (2023).

[50] V. Kasper, G. Juzeliūnas, M. Lewenstein, F. Jendrzejewski, and E. Zohar, From the Jaynes–Cummings model to non-Abelian gauge theories: A guided tour for the quantum engineer, New J. Phys. **22**, 103027 (2020).

[51] I. Raychowdhury and J. R. Stryker, Loop, string, and hadron dynamics in SU(2) Hamiltonian lattice gauge theories, Phys. Rev. D **101**, 114502 (2020).

[52] Z. Davoudi, I. Raychowdhury, and A. Shaw, Search for efficient formulations for Hamiltonian simulation of non-Abelian lattice gauge theories, Phys. Rev. D **104**, 074505 (2021).

[53] Z. Davoudi, M. Hafezi, C. Monroe, G. Pagano, A. Seif, and A. Shaw, Towards analog quantum simulations of lattice gauge theories with trapped ions, Phys. Rev. Res. **2**, 023015 (2020).

[54] E. Rico, M. Dalmonte, P. Zoller, D. Banerjee, M. Bogli, P. Stebler, and U.-J. Wiese, SO(3) "nuclear physics" with ultracold gases, Ann. Phys. **393**, 466 (2018).

[55] C. Laflamme, W. Evans, M. Dalmonte, U. Gerber, H. Mejía-Díaz, W. Bietenholz, U.-J. Wiese, and P. Zoller, $\mathbb{C}\mathrm{P}(N-1)$ quantum field theories with alkaline-earth atoms in optical lattices, Ann. Phys. **370**, 117 (2016).

[56] D. Banerjee, S. Caspar, F.-J. Jiang, J.-H. Peng, and U.-J. Wiese, Nematic confined phases in the U(1) quantum link model on a triangular lattice: Near-term quantum computations of string dynamics on a chip, Phys. Rev. Res. **4**, 023176 (2022).

[57] D. Marcos, P. Widmer, E. Rico, M. Hafezi, P. Rabl, U.-J. Wiese, and P. Zoller, Two-dimensional lattice gauge theories with superconducting quantum circuits, Ann. Phys. **351**, 634 (2014).

[58] A. Kruckenhauser, R. van Bijnen, T. V. Zache, M. Di Liberto, and P. Zoller, High-dimensional SO(4)-symmetric Rydberg manifolds for quantum simulation, Quantum Sci. Technol. **8**, 015020 (2023).

[59] D. González-Cuadra, T. V. Zache, J. Carrasco, B. Kraus, and P. Zoller, Hardware Efficient Quantum Simulation of Non-Abelian Gauge Theories with Qudits on Rydberg Platforms, Phys. Rev. Lett. **129**, 160501 (2022).

[60] M. Aidelsburger, L. Barbiero, A. Bermudez, T. Chanda, A. Dauphin, D. González-Cuadra, P. R. Grzybowski, S. Hands, F. Jendrzejewski, J. Jünemann, G. Juzeliūnas, V. Kasper, A. Piga, S.-J. Ran, M. Rizzi, G. Sierra, L. Tagliacozzo, E. Tirrito, T. V. Zache, J. Zakrzewski *et al.*, Cold atoms meet lattice gauge theory, Philos. Trans. R. Soc. A **380**, 20210064 (2022).

[61] R. Dasgupta and I. Raychowdhury, Cold-atom quantum simulator for string and hadron dynamics in non-Abelian lattice gauge theory, Phys. Rev. A **105**, 023322 (2022).

[62] S. Notarnicola, M. Collura, and S. Montangero, Real-time-dynamics quantum simulation of $(1+1)$-dimensional lattice QED with Rydberg atoms, Phys. Rev. Res. **2**, 013288 (2020).

[63] A. F. Shaw, P. Lougovski, J. R. Stryker, and N. Wiebe, Quantum algorithms for simulating the lattice Schwinger model, Quantum **4**, 306 (2020).

[64] A. Ciavarella, N. Klco, and M. J. Savage, Some conceptual aspects of operator design for quantum simulations of non-Abelian lattice gauge theories, arXiv:2203.11988.

[65] J. F. Haase, L. Dellantonio, A. Celi, D. Paulson, A. Kan, K. Jansen, and C. A. Muschik, A resource efficient approach for quantum and classical simulations of gauge theories in particle physics, Quantum **5**, 393 (2021).

[66] A. M. Childs, Y. Su, M. C. Tran, N. Wiebe, and S. Zhu, Theory of Trotter Error with Commutator Scaling, Phys. Rev. X **11**, 011020 (2021).

[67] E. A. Martinez, T. Monz, D. Nigg, P. Schindler, and R. Blatt, Compiling quantum algorithms for architectures with multi-qubit gates, New J. Phys. **18**, 063029 (2016).